Asian Journal of Pharmaceutical Sciences 17 (2022) 596–609

Available online at www.sciencedirect.com

ScienceDirect

journal homepage: www.elsevier.com/locate/AJPS

Original Research Paper

Design, preparation and pharmacodynamics of ICG-Fe(III) based HCPT nanocrystals against cancer

Qiongzhe Ren[a,1], *Xuefeng Tang*[b,1], *Yi Lu*[c], *Qing Li*[a], *Zhiqian Liao*[a], *Shinan Jiang*[a], *Haoli Zhang*[d], *Zhigang Xu*[c], *Lei Luo*[a,*]

[a] *College of Pharmaceutical Sciences, Southwest University, Chongqing 400715, China*
[b] *Department of Pathology, Chongqing General Hospital, University of Chinese Academy of Sciences, Chongqing 401120, China*
[c] *School of Materials and Energy and Chongqing Engineering Research Center for Micro–Nano Biomedical Materials and Devices, Southwest University, Chongqing 400715, China*
[d] *State Key Laboratory of Applied Organic Chemistry (SKLAOC), College of Chemistry and Chemical Engineering, Key Laboratory of Special Function Materials and Structure Design (MOE), Lanzhou University, Lanzhou 730000, China*

ARTICLE INFO

Article history:
Received 21 February 2022
Revised 2 May 2022
Accepted 14 May 2022
Available online 18 June 2022

Keywords:
Nanocrystal
Stabilizer-free
Stimuli-responsive
Drug delivery
Combination therapy

ABSTRACT

The use of nanocrystal technology to manufacture drug delivery systems intended to enhance therapeutic efficacy has attracted the attention of the pharmaceutical industry. However, the clinical application of nanocrystal drugs for injection is restricted by Ostwald ripening and the large-scale use of stabilizers such as polysorbate and lecithin, which have potential toxicity risks including hemolysis and allergies. Here, we designed an amorphous nanocrystal drug complex (IHNC), which is stabilizer-free and composed of indocyanine green (ICG) framework loading with a chemotherapeutic agent of 10-hydroxycamptothecin (HCPT). Considering the possibility of industrial manufacturing, IHNC was simply prepared with the assistance of ferric ion (III) *via* supramolecular assembly strategy. The theoretical result of Materials Studio simulation indicated that the prepared ICG-Fe(III) framework showed a stable spherical structure with the appropriate cavity for encapsulating the two drugs of HCPT and ICG with equal mass ratio. The IHNC was stable at physiological pH, with excellent PTT/PDT efficacy, and *in vivo* probing characteristics. The nanoscale size and reductive stimuli-responsiveness can be conducive to drug accumulation into the tumor site and rapid unloading of cargo. Moreover, such combination therapy showed synergistic photo/chemotherapy effect against 4T1 breast cancer and its tumor inhibition rate even up to 79.4%. These findings demonstrated that the nanocrystal drug delivery strategy could avoid the use of stabilizers and provide a new strategy for drug delivery for combination therapy.

* Corresponding author.
E-mail address: drluolei@swu.edu.cn (L. Luo).
[1] These authors contributed equally to this work.
Peer review under responsibility of Shenyang Pharmaceutical University.

https://doi.org/10.1016/j.ajps.2022.05.001

1. Introduction

Nanocrystal technique is derived from nanotechnology and pharmacy that greatly improved the *in vivo* behavior such as oral bioavailability and distribution of poorly soluble drugs, eventually reaching a nano-state with the assistance of stabilizers [1,2]. By contrast with nanoparticles prepared by macromolecular tangled methods [3,4], nanocrystal is normally carrier-free with solubilization and better stability [5]. However, there are two main factors affecting the application of nanocrystal drugs: (1) Incapable of controlled drug release in the site of action, which could inevitably bring toxicity to normal tissues [6]. (2) Use of a large portion of stabilizers during the preparation process, which leads to hemolysis and potential side effects [7,8]. According to the Handbook of Pharmaceutical Excipients, including 2-pyrrolidone and sodium dodecyl sulfate, which are severely restricted for intravenous use [9,10]. For example, polysorbate in drug formulations has been implicated in many reactions (*e.g.*, hypersensitivity, nonallergic.) and injection-site adverse events (*e.g.*, pain, erythema, thrombophlebitis). In practice, the *in vivo* and *in vitro* correlation (IVIVC) is difficult to establish after intravenous administration of nanocrystal owing to either short residence time or fast precipitation [11].

Drug release at the site of action is the major challenge in the nanocrystal drug delivery process, and its common release behavior is sustained instead of controlled relying on specific lesion conditions [12]. A series of responsive nanomedicines are triggered by tumoral intracellular microenvironment stimuli (acidic pH, reactive oxygen species and high GSH level, etc.), have been vastly studied [13–16]. The expression of GSH (2–10 mmol/l) in tumor cells (ovarian, colon, breast cancer, lymphoma, etc.) is 1000 times higher than extracellularly [17–19]. Chemical bonds such as selenium bond, succinimide sulfide bond, and disulfide bond, as well as metal ions with strong oxidation ability such as Fe(III) and Ag(I), were smartly bridged among drugs to form nanocrystals. The high level of strong reductivity of GSH in tumor cells could break the linked internal force thereby controlling drug release [20].

To overcome the challenge of toxic side effects caused by stabilizers, new types of nanocrystal techniques have been extensively studied. It was reported that novel nanocrystal preparation technologies such as micro fluidization, aerosol solvent extraction, and evaporative precipitation into aqueous solution were developed to reduce the use of stabilizers [21]. However, the further clinic application is still limited by the complicated manufacturing process and screening inefficiency. Amorphous coordination polymer particles (ACPPs) provide a simplified preparation strategy that shows advantages including tailorable nanocrystal size and structure, as well as well-defined pore aperture. The organic linker of ACPPs can be either a variety of metal ions or commercially, available chemical drugs with simple and mild conditions [22,23]. It is interesting that the two sulfonate anions of ICG readily react with some metal ions such as the Fe(III) [24,25], a necessary metal ion in the body and can be reduced by GSH in the tumor microenvironment. Many researchers have previously investigated the application of iron-based ICG in photothermic therapy, where Liao constructed a multimodal imaging-guided synergistic cancer photo-immunotherapy by employing a specific MOF (MIL101-NH2) as the core carrier, etc. [26–28]. which underpin us envision of constructing metal-ligand organic frameworks for drug delivery, and support the effectiveness of iron-based ICG for combined PDT/PTT/chemotherapy. The formed ICG-based ACPPs (ICG-ACPPs) will prolong blood circulation and realize control release. Moreover, the cavity of ICG-ACPPs is capable of carrying hydrophobic molecules to form nanocrystal drug complexes without stabilizers [29,30].

In this study, we designed an amorphous nanocrystal drug complex (IHNC) of ICG and HCPT, which were used in the integration of chemotherapy, photothermal and photodynamic therapy to enhance anti-tumor efficacy (Scheme 1). Firstly, Materials Studio Modeling (MS, version 6.0, Accelrys) simulated the structure, ICG-Fe(III) framework was formed by Fe ion and ICG through coordination bonds between multidentate organic linkers and metal cations [31]. Specifically, the ratio of Fe ions was screened to obtain the optimized voids and framework structure. Then, IHNC was prepared by a 'drug-drug self-assembly' strategy with ICG-Fe(III) and HCPT. ICG-Fe(III) was characterized by transmission electronic microscope (TEM), scanning electron microscope (SEM), Energy Dispersive Spectroscopy (EDS), Circular dichroism (CD), and X-Ray photoelectron spectroscopy (XPS). Dose-response matrices were used to calculate the combination index (CI) and the inhibitory effect on metastasis/invasion of IHNC was evaluated on 4T1 murine breast cancer cells. The *in vivo* distribution, pharmacokinetics, anti-cancer efficacy, and anti-metastasis of IHNC were evaluated on breast cancer mice and healthy SD rats. The results demonstrated the decent anti-cancer efficacy of IHNC and the simplified preparing method could potentially be applied to large-scale production by accelerating laboratory-to-clinic-to-industry translation.

2. Materials and methods

2.1. Materials

$FeCl_3 \cdot 6H_2O$, 10-hydroxycamptothecin (HCPT), and indocyanine green (ICG) were purchased from Aladdin (China). 2, 7-dichlorofluorescein diacetate (DCFH-DA), N, N-Dimethyl formamide (DMF), dimethyl sulfoxide (DMSO), and chloroform were supplied by Sigma-Aldrich (USA), Annexin V-FITC/PI staining kits were purchased from Life Technologies (China). The elemental analysis results were obtained from Thermo ESCALAB 250Xi (USA), The UV–vis spectrum was recorded on a UV-6100 spectrophotometer (Shanghai Mapada Instruments, China). Fluorescence imaging in mice was carried out by the NIR imaging system (IVIS Lumina Kinetic Series III, PerkinElmer, USA), Microscopy images were captured by confocal laser scanning microscope (CLSM; LSM-800, ZEISS, DEU).

2.2. Cells and animals

The 4T1 murine breast cancer cell line was obtained from the Chinese Academy of Science Cell Bank for Type Culture

Collection (China). Cells were propagated in the DMEM (1% streptomycin and 1% penicillin came from Sigma-Aldrich, USA) media containing 10% heat-inactivated fetal bovine serum (FBS, Hyclone, USA) at 5% CO_2, 37 °C. Female BALB/c (20 ± 2 g, 6–8 weeks), Kunming mice (20 ± 2 g, 6–8 weeks), and SD rats (200 ± 5 g, 6–8 weeks) were purchased from HFK Bioscience, Beijing. All the animal experiments were approved by the Institutional Animal Care and Treatment Committee of Southwest University.

2.3. Structure simulation

A three-dimensional (3D) model of the proposed structure of our porous ICG-Fe(III) framework was established by Materials Studio Modeling (version 6.0, Accelrys), which was optimized by using the CASTEP module in Materials Studio [32]. The surface area of ICG-Fe(III) was carried out using the "Atom, Volumes and Surface" module in Materials Studio. A grid interval of 0.1 Å was used for all the surface area calculations. The accessible solvent surface areas were calculated from a simple Monte Carlo integration technique where the probe molecule was "rolled" over the framework surface. The radius of the probe molecule was 1.82 Å, which was the kinetic radius of N_2 [33].

2.4. Characterization of ICG-Fe(III)

CD was used to detect the configuration and conformation of molecules at different feeding ratios of Fe(III) and ICG, and detect 1:1, 1:20, 1:50, and 1:100, we calculated the anisotropy factors (g_{CD}) of the CD absorption (θ, mdeg) of ICG-Fe(III) based on Equation 1 [34,35]. Respectively. XPS was carried out to analyze the oxidation states and content ratio of ICG and Fe. Finally, the nano-sized structure was examined by TEM.

$$g_{CD} = \frac{\Delta A}{A} = \frac{\theta(mdeg)}{32982 * A} \quad (1)$$

where ΔA is the absorption difference between the left-handed and right-handed spin- polarized light, A is the total absorption of the unpolarized light.

2.5. Preparation of nanocrystal drug complex IHNC

IHNC was prepared similarly to the Bottom-up method [36]. First, ICG was dissolved in a solution (methanol: water=2:1, v/v), and then Fe(III) was added, the solution was stirred for 3 h at room temperature. Next, HCPT was dissolved in an organic solution containing DMSO and chloroform. Under ultrasonic conditions, the mixed solution containing ICG was slowly added to the organic solution containing HCPT, and after 5 min of ultra-sonication, the solution above was taken out and left to sit for 5 min. Finally, the organic solvent was removed by rotary evaporation at 60 °C, after water was removed by freeze-dried, the product was collected.

2.6. Characterization of IHNC

TEM (JEM-1200EX, the accelerate voltage was 100 kV; dot resolution was 0.14 nm, the copper mesh was used for sample preparation and photographed the topography) was applied to observe the morphology of IHNC. SEM (SU8020, SEM was coupled with Energy Dispersive Spectroscopy, the accelerate voltage was 3 kV; sputtering time was 60 s). The hydrated particle size of IHNC were measured with a dynamic light scattering (DLS) Zeta-sizer (Malvern Instruments, Malvern, UK) at a wavelength of 633 nm at 25 °C. Each sample was measured 13 runs per measurement and 15 s per run. Distinct fractions of the runs were removed from the final measurement calculation using a dust filtration algorithm. The intensity-weighted harmonic mean particle diameter (Z-average) and the polydispersity index (PI) according to ISO 22412 were used to compare sizes and size distributions of the different samples. Each measurement was performed in triplicate. X-ray diffraction (XRD) was recorded on an XD-6 X-ray diffractometer with Cu Kα radiation ($\lambda = 1.54056$ Å) and operated at a generator voltage of 36 kV, an emission current of 20 mA and scanning speed of 8°/min, UV-6100 spectrometer (wavelength range from 200 to 1000 nm) and Agilent 1200 (HPLC, high-performance liquid chromatography, columns where 150 mm in length with matched retention factors, the mobile phase was comprised of various ratios of acetonitrile (27%) and water (73%, pH=3.0) so that the retention factors would be matched, the detection was performed using UV at a wavelength of 384 nm) were used to prove the successful loading of ICG and HCPT. The drug loading capacity (DL) was determined according to the following formula:

$$DL(\%) = (M_t - M_u)/M_s \times 100\%$$

Where M_t, M_u, M_s were the amount of loaded drug, the amount of un-encapsulated drug, and the total amount of IHNC, respectively.

2.7. In vitro drug stability while PDT oxidization

IHNC was irradiated for 10 min (808 nm, 1 W/cm^2), the content and structural stability of HCPT were recorded by Agilent 1200. IHNC was added to DMEM containing 10% FBS, and the size within 9 d was recorded by ZEV3600.

2.8. In vitro drug release

IHNC was added to the dialysis bag (MWCO: 3500 Da) and gently shook at 110 RPM in a shaker with different concentrations of glutathione (GSH, 0 mmol/l, 2 mmol/l) under 37 °C. At a predetermined interval, 1 ml dialysate was taken out, and then the corresponding fresh PBS solution of the same volume was added, the release amount of HCPT was measured by UV-6100.

2.9. In vitro photothermal properties

PBS, free ICG, IHNC solutions (C_{ICG}: 30.00 μg/ml, C_{HCPT}: 30.61 μg/ml) were irradiated with laser irradiation (808 nm, 1 W/cm^2, 5 min), and the temperature change of the solution was recorded every minute. The thermal infrared imaging camera (FLIR E95, FLIR Systems) was used to record the infrared thermogram. To study the photothermal effect of

IHNC, a solid-state laser source with a wavelength of 808 nm was applied to irradiate the samples. IHNC (C_{ICG}: 10, 20, 30, 40 μg/ml) samples were irradiated for 5 min (808 nm, 1 W/cm^2) and a fix concentration of IHNC (C_{ICG}: 30 μg/ml) was exposed under different laser intensities (0.5, 1.0, 1.5, 2.0 W/cm^2) for 5 min. In addition, the photothermal stability of IHNC (C_{ICG}: 40 μg/ml) was confirmed by cyclic irradiation experiments (808 nm, 1 W/cm^2, 5 min), and the external thermogram and temperature were recorded by FLIR E95.

2.10. Cell viability assay

To evaluate the survival rate of cells under different concentrations of ICG and HCPT, the cell viability was assessed by the Cell Counting Kit-8 (CCK-8) assay. Furthermore, Synergy Finder was used to screening the appropriate ratio to achieve the best synergistic therapeutic effect, and then Compusyn was used to analyze the CI of the two drugs.

In brief, 4T1 cells at the exponentially growing phase were seeded on 96-well plates at 5×10^3/well and cultured overnight. These cells were treated with ICG (with/without laser irradiation, 808 nm, 1 W/cm^2, 5 min), HCPT, IHNC (with/without laser irradiation, 808 nm, 1 W/cm^2, 5 min) at different concentrations. After treatment for 24 h, 100 μl fresh medium containing 10% (v/v) of CCK-8 was added to the wells, and the plates were incubated for an additional 2 h in the dark. Finally, the absorbance was measured at 450 nm using a microplate reader. Moreover, the staining of living/dead cells was also used to characterize the toxicity of IHNC (C_{ICG}: 20 μg/ml). 1×10^5 4T1 cells / well were added to a 12-well plate. The culture medium containing free ICG, free HCPT, IHNC were added to different wells for 4 h. After irradiation treatment, the cells were cultured for 20 h. Finally, the cells in each well were stained with the Living/Dead cell double staining kit (Live Dye: Ex/Em=488/530 nm) and Nuclei Dye: Ex/Em=535/617 nm) for 20 min, and a fluorescence microscope was used to take images.

2.11. Evaluation of ROS generation in vitro

ADPA (10 mM) was used to detect the production efficiency of singlet oxygen in the solution. The solutions containing ICG or IHNC (C_{ICG}: 3.93 μg/ml) were irradiated by laser irradiation (808 nm, 1 W/cm^2, 10 min), and the absorbance changed at 400 nm was recorded by UV–Vis. Cellular ROS levels could be measured by using oxidation-sensitive fluorescent probe DCFH-DA, and the fluorescence intensity was observed and photographed under CLSM. 5×10^4 4T1 cells / well were added to a 12-well plate and were cultured at 37 °C for 12 h. The culture medium containing ICG, HCPT, and IHNC (C_{ICG}: 20 μg/ml) was added and incubated for 4 h. the cells were incubated for another 2 h after adding DCFH-DA (10 μM). then treated with laser radiation (808 nm, 1 W/cm^2) for 5 min to allow the DCFH-DA to react with the generated ROS for 30 min. After washing cells with PBS, the nuclei were stained with Hoechst 33342 for CLSM observation (λ_{ex}=488 nm and λ_{em}=505–525 nm for DCF; λ_{ex}=405 nm and λ_{em}=440–480 nm for Hoechst 33342) after washing cells with PBS.

2.12. Cellular uptake of IHNC

The cellular uptake of IHNC was measured by flow cytometry. 4T1 cells were seeded on a 24-well plate for 12 h, and the culture medium containing IHNC (C_{ICG}: 10 μg/ml) was added to the well plate for 0.15 h, 0.5 h, 1 h, 2 h, 4 h, and then measured by flow cytometer (Ex=740 nm and Em=790 nm).

For further quantitative analysis of cellular uptake of IHNC, we also conducted fluorescence measurements. The cytoskeleton of cells was stained by AF-488 (Ex=495 nm, Em=519 nm), then the fluorescence of HCPT and ICG were captured. The intracellular localization of IHNC was analyzed by CLSM. Briefly, 4T1 cells were cultured on a 12-well plate, and the cells were incubated with IHNC (C_{HCPT}: 20 μg/ml) for 1 h and 4 h, respectively. Then, the lysosomes were stained with lysosomal Green DND-22 (LyG, Ex=373 nm, Em=422 nm) for 30 min, and the mitochondria were stained with mitochondrial green FM (MTG, Ex=490 nm, Em=516 nm) for 30 min, and the fluorescence images were captured by CLSM.

2.13. Penetration effect of IHNC in MCSs

100 mg agarose was added to 10 ml 1x TEA buffer, and the solution containing agarose was added to a 96-well plate with 100 μl per well, and then, 4T1 cells 1×10^3 4T1 cells/well were added to a 96-well plate for 4 d incubation to form tumor multicellular spheroids (MCSs). Finally, the MCSs were cultured for 6 h in the medium containing IHNC (C_{HCPT}: 20 μg/ml), and the penetration of the drug in MCSs was captured by CLSM.

2.14. In vivo imaging and biodistribution

The 4T1 cells (5×10^5 in 100 μl) were used for establishing subcutaneous breast cancer-bearing models by injecting them at the right legs of the female BALB/c mice. About 2–3 weeks after tumor implantation, mice were intravenously injected with ICG and IHNC (C_{ICG}: 5 mg/kg) at different times after injection (6, 12, 24 and 36 h). The fluorescence signals were acquired by PerkinElmer IVIS Lumina Kinetic Series III (Ex=740 nm and Em=790 nm). Furthermore, the mice were sacrificed at 24 h, the tumors and major organs (hearts, livers, spleens, lungs, and kidneys) were collected and captured.

2.15. Pharmacokinetics of IHNC and HCPT injection

The HCPT injection and IHNC were administered *via* the tail vein at an HCPT dosage of 4 mg/kg body weight. Blood was collected at the following time points: 5, 10, 20, 30, 45, 60, 120, 240 and 480 min, and blood was collected. Plasma was then collected by centrifugation for 5 min. Add 10% phosphoric acid, methanol, and ether solution to the plasma sample, vortex, and stand for 60 min to ensure complete cyclization of HCPT. The supernatant was centrifuged and collected. After drying with nitrogen, it was re-dissolved with methanol, the content of HCPT in the supernatant was analyzed by HPLC. The HPLC method was described in 2.6.

Table 1 – Dosage regimen.

Groups	ICG (mg/kg)	HCPT (mg/kg)	Laser irradiation
Control	N/A	N/A	No
ICG+Laser	4.9	N/A	808 nm
HCPT	N/A	5.0	No
IHNC	4.9	5.0	No
IHNC+Laser	4.9	5.0	808 nm

2.16. Blood routine examination

Kunming mice were randomly divided into two groups with 6 mice in each group and injected with PBS and IHNC (C_{HCPT}: 5 mg/kg) respectively. After the administration, blood was collected on the 1_{st}, 7_{th}, and 14_{th} d to test the blood biochemical blood routine. Moreover, the blood was taken from the eyeball and the red blood cell were obtained by centrifugation. The PBS and TritonX-100 were served as negative control and positive control, respectively. The absorbance of IHNC (C_{HCPT}: 1, 2, 5, 10, 25, 50, 100 μg/ml) at 577 nm was detected and the hemolysis calculation formula was as follows:

Hemolysis (%)=(Ab_{sample}-$Ab_{negative}$)/($Ab_{positive}$-$Ab_{negative}$) x 100%

2.17. In vivo anti-tumor efficacy and histological studies

We constructed the same ectopic model of breast cancer as described above. When tumors reached approximately 100–150 mm^3 (1–2 weeks after implantation), mice were randomly divided into five groups with 6 mice in each group, then the mice were injected with PBS, ICG, HCPT, and IHNC respectively (Table 1), of which ICG+L (with laser irradiation), IHNC (with and without laser irradiation). The drugs were administered *via* the tail vein every 4 d for a total of 3 times, with laser irradiation for 24 h after administration. During the treatment, the tumor volume (length × $width^2$ × 0.5) and body weight were measured every day. All mice were sacrificed on Day 16, tumors and major organs such as hearts, livers, spleens, lungs, and kidneys from models were excised and fixed for slicing. The sections were stained using hematoxylin and eosin (H&E) for histopathological evaluation and the other part of the paraffin tumor section was stained for TUNEL.

2.18. Statistical analysis

All the experiments were repeated at least three times and data were expressed as mean ± standard deviation (SD) by using student *t*-test, * P <0.05 was considered significant, ** P <0.01 was very significant, and *** P <0.001 was highly significant.

3. Results and discussion

3.1. Preparation and characterization of ICG-Fe(III)

ICG-Fe(III) was constructed by coordinating ICG with Fe(III) in solution and it was applied as a vehicle for further drug loading. The mass ratio of Fe(III) to ICG was calculated by using the CASTEP module in Materials Studio, and it was showed that the most stable spatial structure when the mass ratio of Fe to ICG was 1:41.50 (*i.e.*, Fe to ICG molar ratio of 1:3). In addition, the occupied volume (Å^3) of the nanoparticle was calculated to be 21,032.33, and the volume of the drug-loaded cavity (Å^3) was 31,511.29. In Fig. 1B, the framework is formed by the coordination of Fe and ICG, and the gray part is the solvent accessible surface and the white is the cavity (Fig. 1B). TEM images of ICG-Fe(III) showed uniformed porous morphology (165 nm average size) at the ratio (m_{Fe}:m_{ICG} 1:50), which further confirmed the simulated 3D model (Fig. 1B and 1C), and when the proportion of Fe was relatively large (m_{Fe}:m_{ICG}=1:1), the structure could not be effectively formed, and there was no suitable cavity for subsequent drug loading when the proportion of ICG was excessive (m_{Fe}:m_{ICG}=1:100). CD is a phenomenon whereby a material absorbs more of one circular polarization than the other, making the transmitted light elliptical, the degree of chirality can be represented in terms of ellipticity (θ, in mdeg) or g_{CD}, the CD results showed a significant increase in the polarization signal with the proportion of Fe(III) increasing (Fig. S2),and the results of gCD obtained from circular dichroism show that the gCD at 200–250 nm gradually decreases with decreasing iron content, which can be attributed to the variation in the degree of crystallinity and chirality due to different Fe content (Fig. S3). The above results indicate that Fe(III) could stabilize the crystal skeleton structure. The amount of Fe(III) and relevant element content in the vehicle was evaluated by ICP-OES (Table S1 and S2). Furthermore, ICG-Fe(III) was measured by XPS to determine the composition and valence of Fe. The survey spectrum demonstrated that the sample was composed of C, S, N, O, and Fe atoms (Fig. 1A) [37]. The nanocrystals were analyzed using SEM coupled with EDS to confirm the composition and morphology of IHNC. The distribution of elements can be observed in the point-scan mapping of the captured region (Fig. S6A). An EDS-face from a single nanocrystal from the image in Fig. S6B was shown by a solid white box, the elemental mapping of IHNC also reveals that the nanostructure was composed of different fragments, the full coverage of Fe reveals the framework structure.

Content of inorganic elements in the drug is crucial in clinic safety. The Food and Drug Administration (FDA), Pharmacopoeia of the People's Republic of China (ChP), and the International Council for Harmonization of Technical Requirements for Pharmaceuticals for Human Use (ICH) have specified the necessity of the inorganic element impurities assessment. Fe is mentioned as other elements in ICH, which the allowed daily exposures have not been established due to their low inherent toxicity. According to the indications, the clinically recommended dosage of Fe is 4–15 mg/kg and each milliliter of injection is not to exceed 50 mg [38–40]. Here, the dose of Fe has ensured the injection safety which is as low as 0.1035 mg/kg.

3.2. Preparation and characterization of IHNC

IHNC was prepared by simply mixing HCPT with ICG-Fe(III) in solution, which was loaded with up to 49% ICG and 50% HCPT, and the PDI was less than 0.3, which indicated that

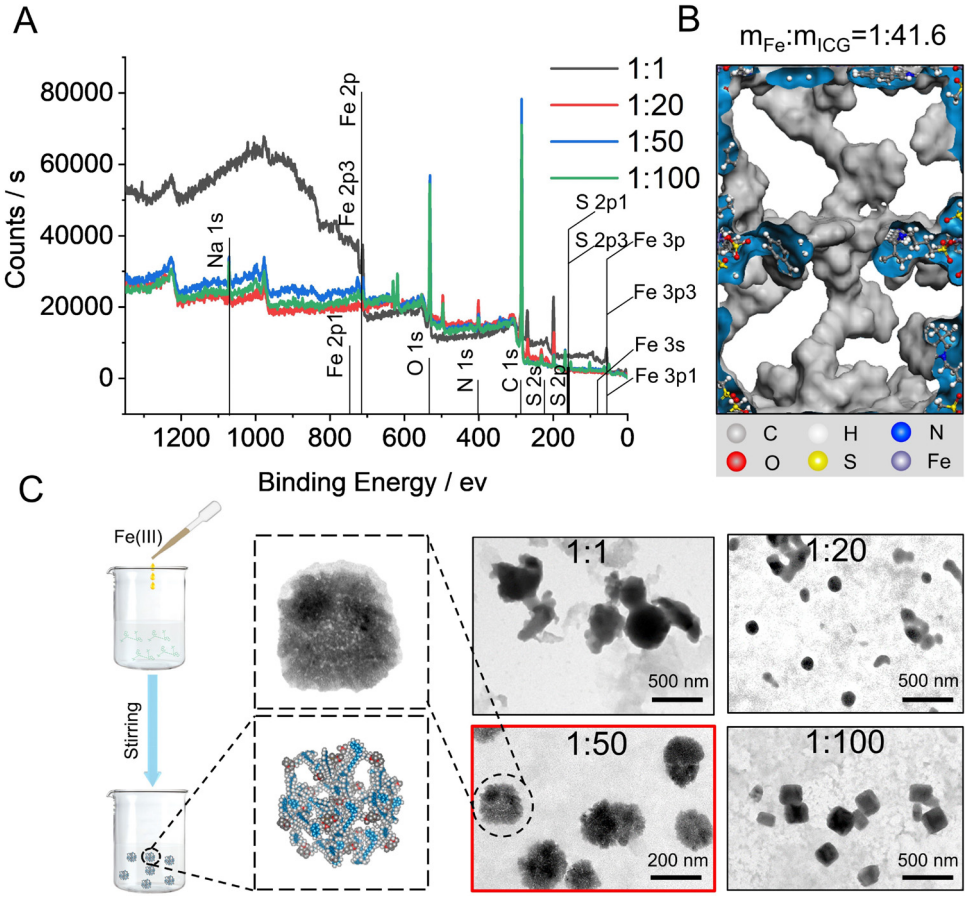

Fig. 1 – Simulation and characterization of ICG-Fe(III). (A) XPS test results of Fe and ICG with different feed mass ratios, (B) the skeleton structure and voids of ICG-Fe(III), (C) schematic diagram of ICG-Fe(III) formation, and TEM images of different feed mass ratios of Fe to ICG.

IHNC could excellently disperse in aqueous [41] (Table S3). To simplify the study, the dosage ratio optimization of ICG and HCPT was simulated by SynergyFinder [42,43]. The results (Fig. 2A) showed that the ZIP synergy score was as high as 10.821 when the ratio was 1:1, and when the synergy scores were larger than 10, the interaction between two drugs was likely to be synergistic. Furthermore, the CI was reportedly simulated by Compusyn [44], and the results showed a strong synergistic potential (Fig. 2B). XRD results showed no obvious diffraction peaks, which proved the amorphous structure of IHNC (Fig. S4). IHNC did not have a fixed lattice structure, but we still simulated the distribution of Fe in IHNC according to VESTA (Fig. S1) The concentration of ICG and HCPT was detected by UV–vis and HPLC (Fig. S7 and S8). The mean hydrodynamic diameter (Dh) of IHNC measured by dynamic light scattering (DLS) was approximately 180 nm (Fig. 2C, m_{ICG}:m_{HCPT}=1:1), which was following the size determined on TEM images (Fig. S9). Such nano-sized particles were conducive to the accumulation at the tumor site by the EPR effect [45].

The stability of IHNC was studied to achieve efficient drug delivery [46]. The variation in particle size of nano-drug was a pivotal exhibition of their stability. It was found that Dh of IHNC was stable in 10% FBS in DMEM at 25 °C for 9 d (Fig. S10A) which indicated that IHNC could have fine stability in biological environments without aggregating. Meanwhile, the zeta potential of IHNC was −14.1 mV (Fig. S10B) and the negatively charged surface could prolong residence time in circulation. The degradation of HCPT rarely happened while the PDT process, which was confirmed by the HPLC analysis (Fig. S11). The results indicated that the *in vivo* PDT treatment would not affect the HCPT stability or change its pharmaceutical effect.

The loading of ICG and HCPT were characterized by UV–vis and fluorescence spectra (Fig. 2D and 2E). It was found that the fluorescence intensity of IHNC decreased by 35.02% compared to the free ICG solution on the ~830 nm when the excitation wavelength was 710 nm. this phenomenon may be related to the ACQ (Aggregation-Caused Quenching, ACQ). Notably, the largest emission peak of the ICG shift from 785 nm to 793 nm when the excitation wavelength was 710 nm, which may be caused by metal-drug organic ligand interactions. Meanwhile, optical photos photographed at UV–vis also explained the result, an obvious shift from 365 to 389 nm was apparent. This result might be attributed to the migration of excitation energy among π-stacked ICG/HCPT molecules as well as the change of molecule conformation in the self-assembly process. Fourier transform infrared spectroscopy

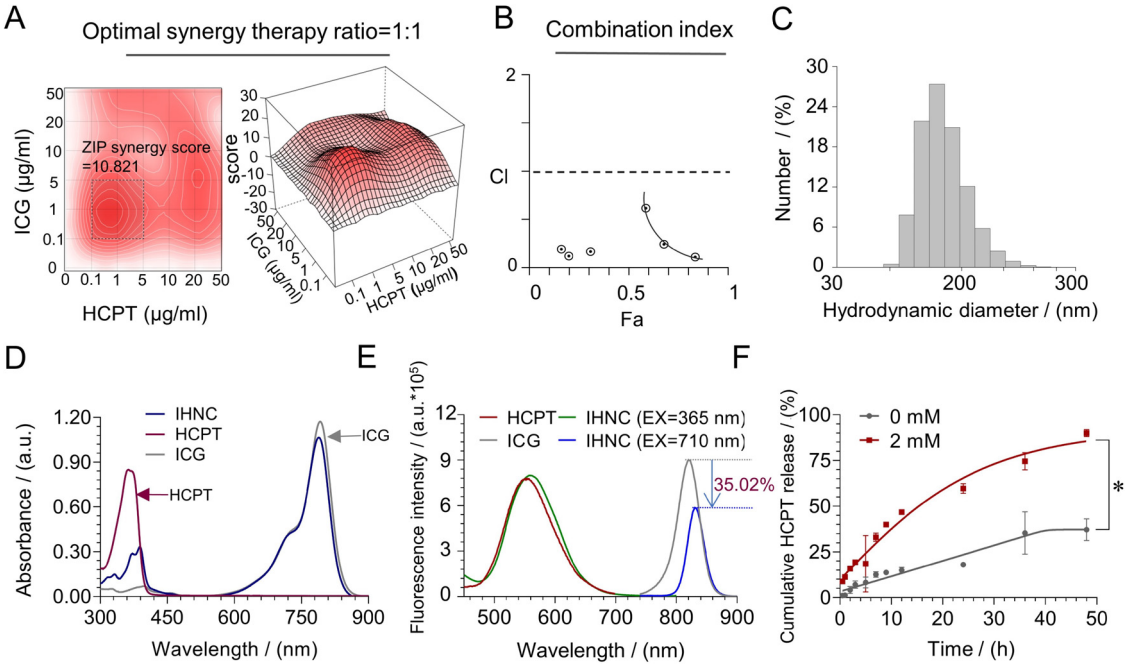

Fig. 2 – Characterization of IHNC. (A) The ratio of ICG and HCPT synergy therapy were screened and analyzed by SynergyFinder. (B) The CI of ICG and HCPT with a mass ratio of 1:1 was investigated, and the data was analyzed by Compusyn. (C) Dh distribution of IHNC. (D) UV–vis-NIR absorption spectra of ICG, HCPT and IHNC. (E) Fluorescence spectra (excitation at 365 nm and 710 nm) of these samples. (F) *In vitro* HCPT released from IHNC in the presence of 0 mM or 2 mM GSH. $n = 3$, error bars represent ± SD, * $P < 0.05$.

(FTIR) further verified the occurrence of this phenomenon based on metal coordination (Fig. S5).

The *in vitro* drug-releasing profiles were performed by the dialysis method. The glutathione (GSH) level in tumor cells was usually 7–10 times higher than that in normal cells. In this assay, GSH was used to simulate the reducing and oxidizing conditions of the tumor microenvironment. As shown in Fig. 2F, HCPT was continuously released with time, and approximately 90% of HCPT was cleaved in the presence of 2 mM of GSH. This release behavior ensured HCPT performed its pharmacological efficacy and prolonged the chemotherapy effect.

3.3. *In vitro photothermic assays*

To assess the photothermic conversion efficiency of IHNC, the photothermic performance of different formulations was conducted upon laser irradiation. The results implied that IHNC retained the original photothermic response compared to free ICG aqueous solution, whereas the temperature increases of saline solution were negligible at the same condition. Moreover, it was found that the maximum temperature of IHNC could reach ~50 °C after irradiation for 5 min (808 nm, 1 W/cm^2). It showed that IHNC could utilize light energy more effectively to convert it into temperature (Fig. 3B). IHNC displayed concentration and power-dependent photothermic effect (Fig. 3C and 3D). To investigate the photothermal stability of IHNC, as shown in Fig. 3E, the photothermal conversion curves of IHNC were obtained under three cycles of irradiation and were shown to remain stable. These results illustrated that this nanocrystal drug could be efficient for further biological applications in photothermic therapy.

3.4. *Cytotoxicity assays*

4T1 murine breast cancer cells have similar growth and metastatic properties to human breast cancer [9], thus they were considered to apply in the following *in vitro* and *in vivo* evaluations. The cytotoxicity was assessed using CCK-8 assay on 4T1 cells which were incubated with free ICG, free HCPT, and IHNC without or with the treatment of NIR laser irradiation (5 min, 1 W/cm^2). IHNC significantly suppressed the tumor cell viability to ~28% and was more effective than free ICG, free HCPT at the same drug concentration (Fig. 4A). The results proved that laser irradiation-induced PDT/PTT had a combined therapeutic effect with chemotherapy, which validated the results of CI screening outcomes. Furthermore, we also carried out the living/dead staining assays (Fig. 4B), and the images have been magnified as Fig. S12 to show a clearer outline of the cells. In this experiment, green and red fluorescence represented live and dead cells, respectively. The IHNC+L (with laser irradiation) treatment group produced the weakest green fluorescence, indicating that the cytotoxicity of IHNC combined with NIR irradiation was significantly higher than other treatment groups. Image J was used for semi-quantitative analysis of living/dead staining experiments results (Fig. S13), which were consistent with cytotoxicity results.

The probe 2′,7′-dichlorofluorescein diacetate (DCFH-DA) was used to determine intracellular ROS. DCFH-DA could be rapidly oxidized to green fluorescent 2′, 7′-dichlorofluorescein

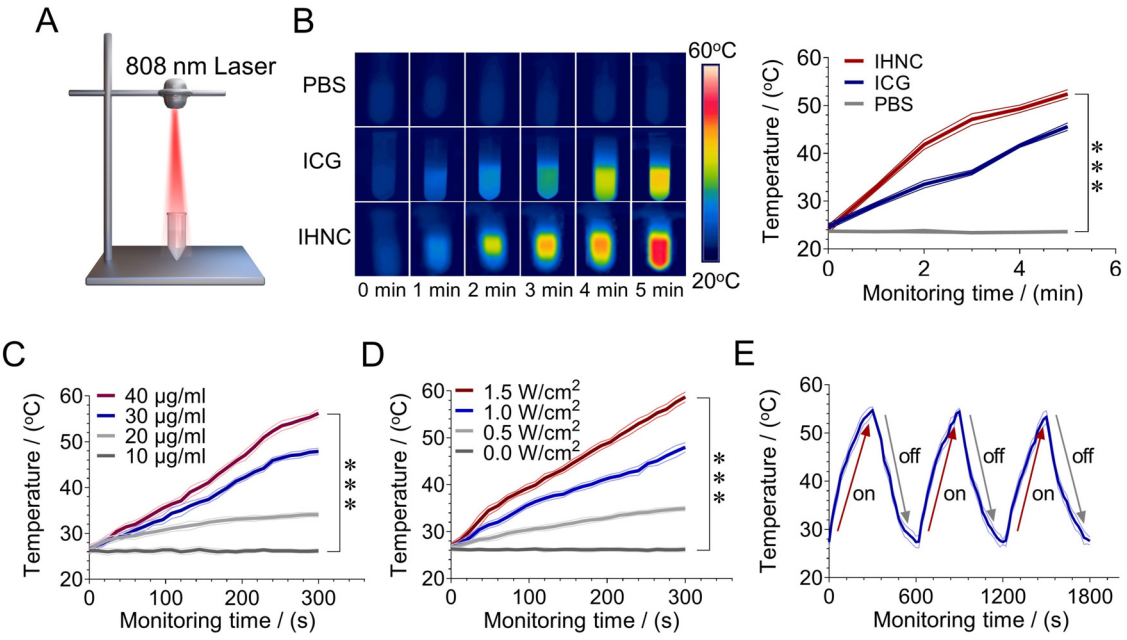

Fig. 3 – *In vitro* photothermic effect of IHNC. (A) Schematic diagram of laser irradiation. (B) Infrared thermal images and the corresponding photothermic effect, C_{ICG}: 30.00 μg/ml, C_{HCPT}: 30.61 μg/ml, 808 nm, 1 W/cm^2. The temperature changes by varying (C) ICG concentrations, 1 W/cm^2, and (D) laser power intensities, C_{ICG}: 30.00 μg/ml. (E) Cycle irradiation experiment, C_{ICG}: 40.00 μg/ml, 808 nm, 1 W/cm^2, $n = 3$, *** $P < 0.001$.

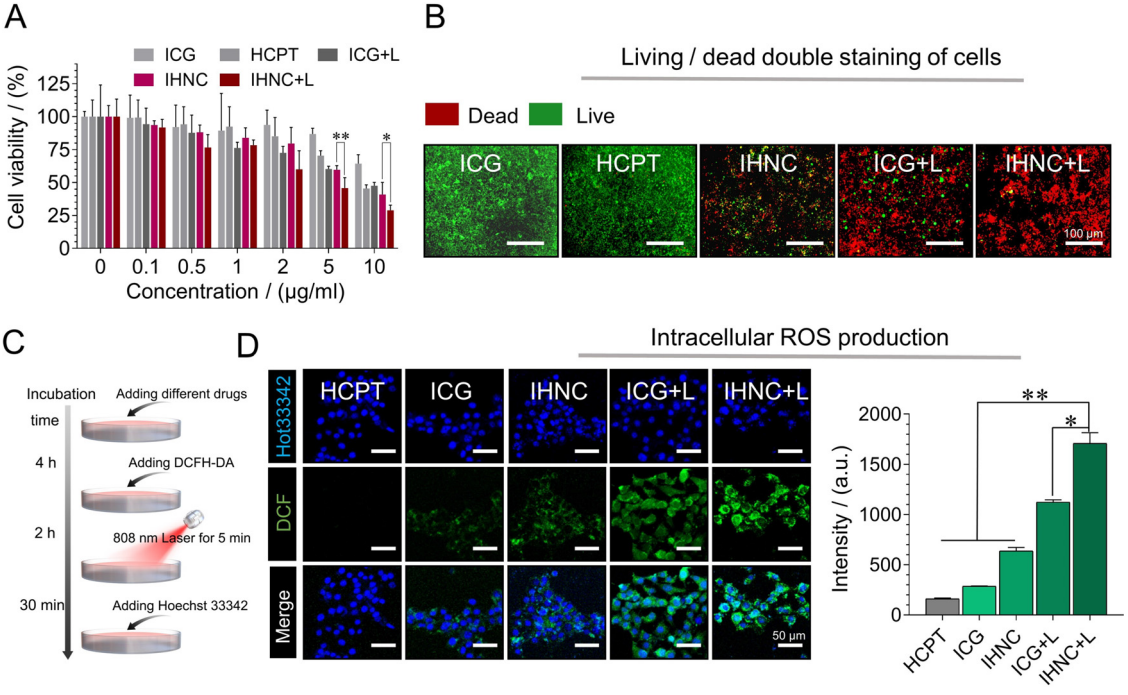

Fig. 4 – Cytotoxicity assays of IHNC. (A) Cell viability of 4T1 cells incubated with free ICG, HCPT, IHNC, and ICG with irradiation, 808 nm, 1 W/cm^2, 5 min. (B) living/dead staining, C_{ICG}: 20 μg/ml, Live Dye: Ex/Em = 488/530 nm and Nuclei Dye: Ex/Em = 535/617 nm. (C) Schematic diagram of DCFH-DA detection process. (D) The CLSM images of ROS production after irradiation and the average fluorescence intensity of DCF, C_{ICG}: 20 μg/ml, λ_{ex}=488 nm and λ_{em}=505–525 nm for DCF; λ_{ex}=405 nm and λ_{em}=440–480 nm for Hoechst 33342. $n = 3$, error bars represent ± SD. *$P < 0.05$, **$P < 0.01$.

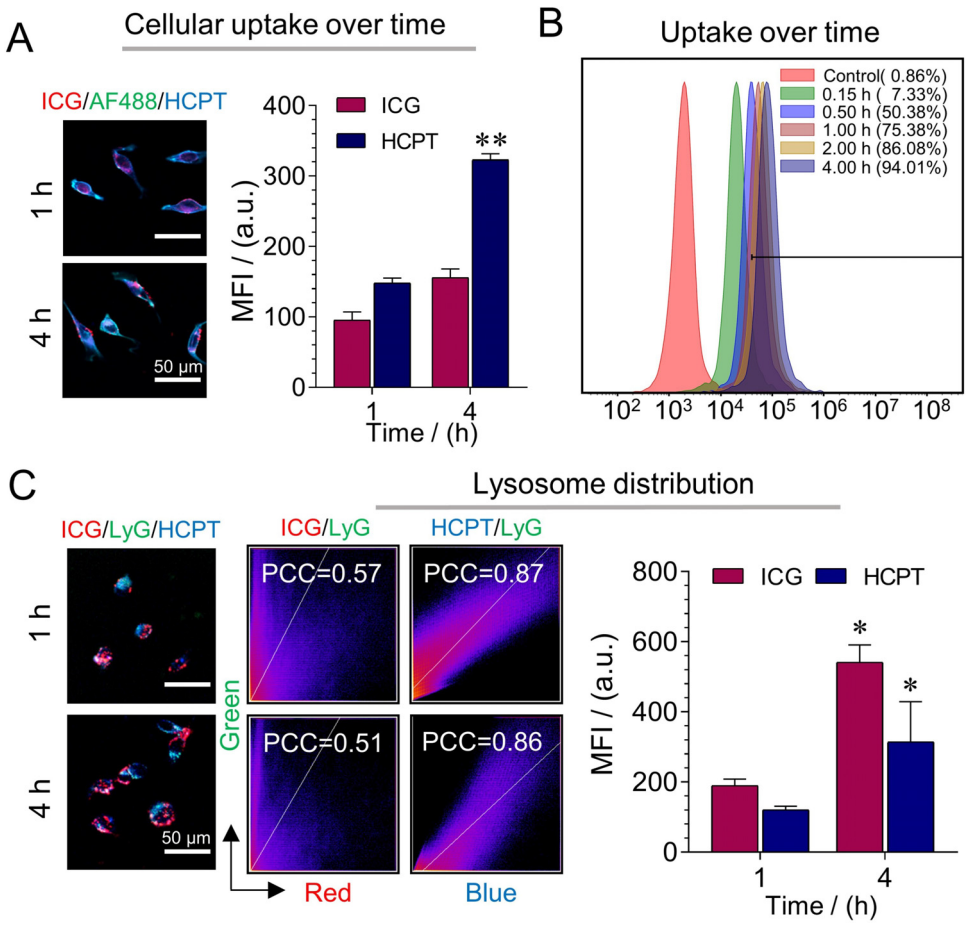

Fig. 5 – Cellular uptake and co-localization of IHNC. (A) The uptake of IHNC was performed by CLSM and (B) flow cytometry, ICG as fluorescence probe, comparing to the fluorescence intensity of HCPT at 1 h, C_{ICG}: 10 μg/ml. (C) The distribution of IHNC and the Pearson correlation coefficient in lysosomes, comparing to the fluorescence intensity of ICG and HCPT at 1 h, C_{HCPT}: 20 μg/ml, AF-488 (Ex=495 nm, Em=519 nm), ICG (Ex=740 nm, Em=790 nm), HCPT (Ex=365 nm, Em=430 nm), lyG (Ex=373 nm, Em=422 nm), MFI: Mean Fluorescence Intensity, $n = 3$, error bars represent ± SD, *$P < 0.05$, **$P < 0.01$.

(DCF). The DCF fluorescence signal of the HCPT control group was extremely weak and negligible, while the cells treated with IHNC had an extremely strong fluorescence signal under laser irradiation, and the quantified results of the fluorescence signal were significantly higher than those of the HCPT group, the ICG group and the unlit IHNC group. (Fig. 4D). ADPA was used to quantitatively singlet oxygen-generating in a test tube. It was observed that IHNC could produce a significantly larger amount of singlet oxygen than that of ICG under laser irradiation conditions (Fig. S14) [47]. The results indicated that IHNC could improve the stability of ICG and be applied as an effective PDT agent against tumor cells. In addition, IHNC might rapidly consume GSH in hypoxic tumor cells during the release of HCPT, resulting in its redox homeostasis imbalance and H_2O_2 accumulation [48], and further induced the increase of intracellular ROS, which verified the effect of combined therapy.

3.5. *Cellular uptake*

The cellular uptake of IHNC was analyzed via CLSM and flow cytometry. The cellular uptake of nanomedicine is directly related to therapeutic efficacy. After incubating the cells with DMEM containing IHNC for 1 h and 4 h, it could be observed that the fluorescence intensity of IHNC-treated 4T1 cells in the cytoplasm gradually increased (Fig. 5A). The flow cytometry results showed that the uptake of IHNC reached up to 94.10% (Fig. 5B). It could be seen that the cellular uptake of IHNC by 4T1 cells was time-dependent, and the quantitative CLSM analysis was consistent with the results (Fig. S15).

As an important fluorescence analysis method, the essence of fluorescence colocalization analysis is to analyze two fluorescent-labeled proteins with independent emission wavelengths and overlapping in space. To determine whether the two proteins were in the same region, that is, whether two different fluorescent molecules appear in the same pixel because of "coincidence" [49], the cell co-localization ability of IHNC was studied. Pearson's correlation coefficient (PCC) was used to quantitatively describe co-localization. In lysosomes (green), the fluorescence intensity of ICG (red) and HCPT (blue) increased simultaneously from 1 h to 4 h, and quantify the average fluorescence intensity of HCPT and ICG within the cell (Fig. 5C). As the incubation time increased, at 1 h and 4 h, the PCC of ICG was 0.57 and 0.51, the PCC of HCPT are 0.87 and 0.86.

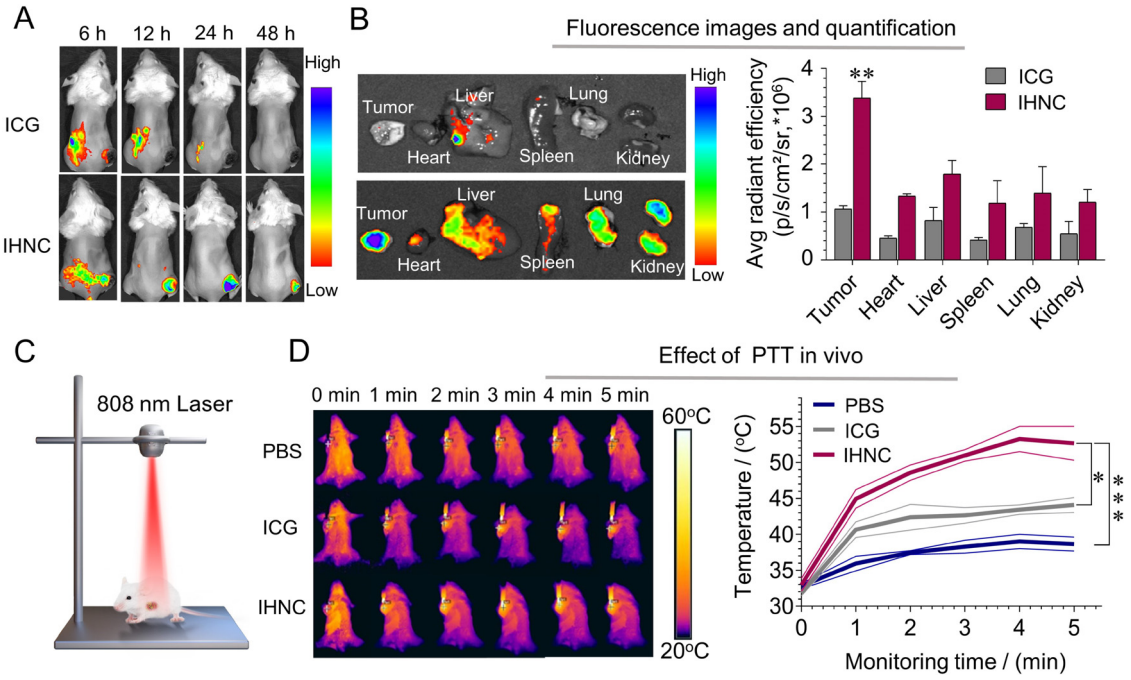

Fig. 6 – Drug targeting and PTT effect *in vivo*. (A) Time-dependent body distribution after *i.v.* injection. (B) Fluorescence image of organs *ex vivo* 24 h after injection, compared to tumors in the ICG group. (C) Schematic diagram of laser irradiation. (D) The thermal imaging and (E) the temperature change of the tumor site, 808 nm, 1 W/cm^2, $n = 3$, error bars represent ± SD, *$P < 0.05$, **$P < 0.01$, ***$P < 0.001$.

The results demonstrated that HCPT was internalized into cells via the lysosome-mediated endocytic pathways. IHNC was disintegrated from GSH stimuli, while ICG and HCPT could be unloaded in the lysosome. ICG was unlikely distributed in lysosomes which might be the amphiphilic ICG molecules diffused into the cytoplasm through the lysosomal membrane [50,51]. The released HCPT remained in the lysosome rather than in mitochondria (Fig. S16).

The nano-size drug has the unique advantage of deep tumor penetration which could enhance treatment results [52]. To simulate and evaluate the penetration ability of IHNC in tumor tissues, 4T1 cells were used to build multicellular spheroids (MCS). which is a three-dimensional model used to study the penetration efficiency of drugs in tumor cells. As shown in Fig. S17, the top layer of MCS observed on the CLSM Z-stack scanning image was defined as 0 μm. At the scanning depth of 60 μm, IHNC treated group showed the strongest fluorescence intensity. There was a tendency for the fluorescence signal distribution of IHNC in tumor cells to first enhance, then weaken and then continue to enhance, and this phenomenon may be caused by the uneven spatial distribution of the drug within the tumor sphere. The results showed that IHNC had a strong tumor penetration and retention ability which increased the cellular uptake and enhanced anti-tumor efficacy.

3.6. *In vivo photothermic effect and biological distribution*

To investigate the biodistribution of IHNC *in vivo*, fluorescence signals of ICG were captured at set time points. The results showed that the free ICG group had a non-obvious tumor-targeting effect within 24 h after the injection (Fig. 6A), on the contrary, a strong signal was observed at the tumor site after the administration of IHNC for 24 h. The results indicated that IHNC was able to accumulate in tumors, which was largely attributed to the EPR effect. We have considered further improving the tumor distribution of such a drug delivery system, and surface modification could assist its active targeting ability. However, the complicated quality control issues limited possible industrial applications. Furthermore, the mice in each group were sacrificed at 24 h and the main organs and tumors were taken to determine fluorescence. The results showed that the tumor fluorescence signal of the IHNC group was significantly higher than that in other groups (Fig. 6B). The liver and kidney had a certain fluorescence intensity, indicating that they might dominate ICG metabolism. Furthermore, the pharmacokinetics of HCPT injection and IHNC were investigated. The analyzing method of HCPT in plasma samples was carefully established and verified (Fig. S18). The results showed that IHNC showed a similar trend in the time-concentration curve by comparing with HCPT injection. IHNC comparatively prolonged the drug resident time in the blood, which could be beneficial to the drug distribution of tumors (Fig. S19A and S19B).

According to the biodistribution results, the laser irradiation time was selected as 24 h, because the fluorescence intensity at the tumor site was the highest. IHNC group showed a significant temperature elevation to 52.7 °C under laser irradiation (Fig. 6D), FLIR E95 was used to record the real-time temperature of the tumor site. It was reported that the cells began to suffer thermal damage when the temperature

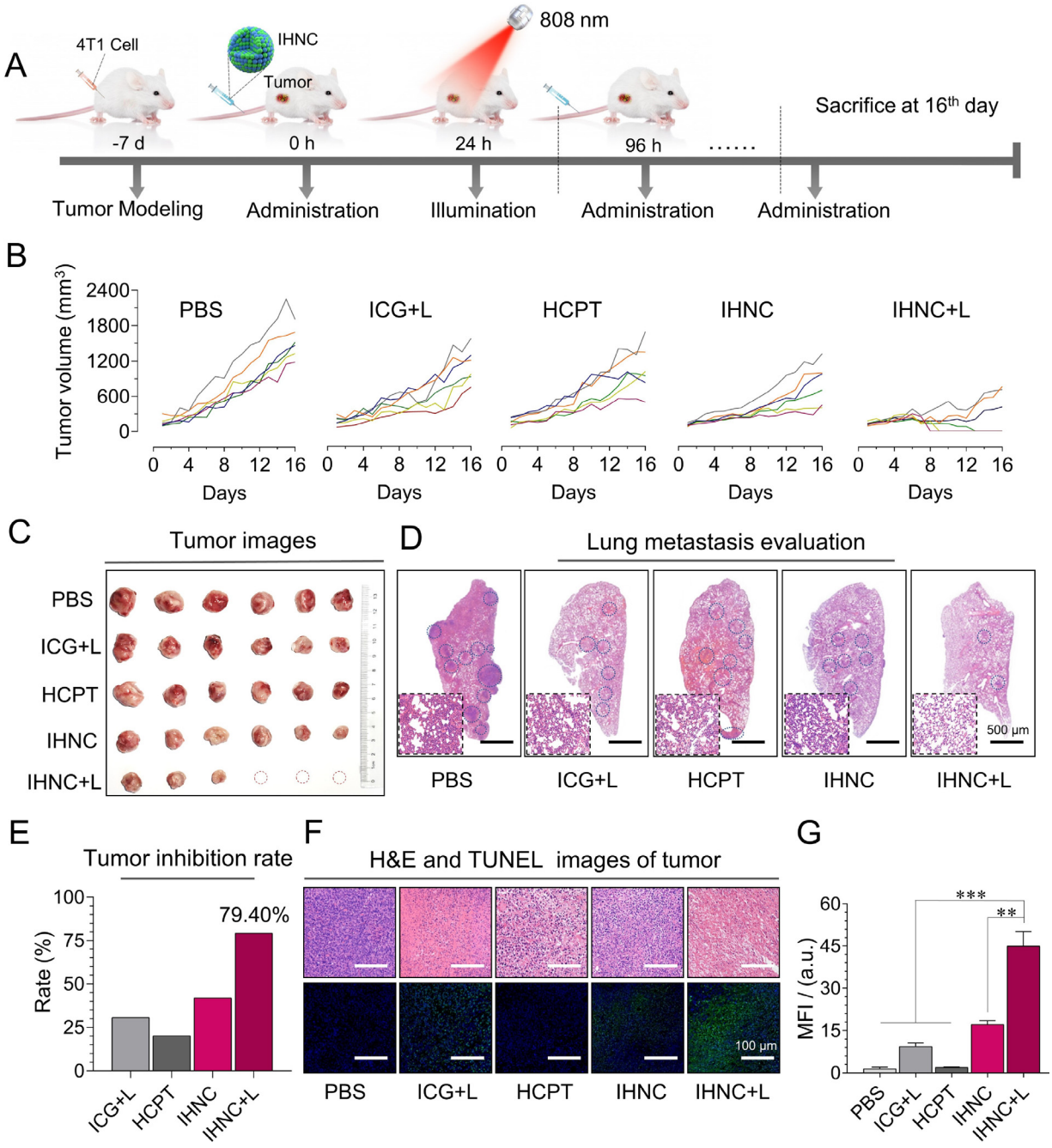

Fig. 7 – *In vivo* anti-cancer efficacy of IHNC. (A) Schematic diagram of administration and treatment. (B) The variation of tumor volume. (C) Harvested mice tumors on day 16, (D) H&E staining of lung metastasis. (E) Tumor inhibition rate of mice. (F) H&E (upper panel), TUNEL (lower panel) staining, and (G) fluorescence of tumor was quantitatively analyzed by image J, $n = 6$, error bars represent ± SD. $^{**}P < 0.01$, $^{***}P < 0.001$.

reaches about 50 °C, collagen degeneration occurred at 55 °C, mitochondria and RNA were destroyed above 60 °C, and tumor cells began to necrosis [53,54]. On the contrary, the tumor temperature of PBS and the free ICG group hardly reached up to 40 °C. IHNC showed a decent photothermic effect *in vivo*, which might be related to energy converting efficiency and targeting distribution.

3.7. *In vivo anticancer efficacy and safety evaluation*

The anti-cancer efficacy of IHNC against breast cancer was evaluated in subcutaneous tumor-bearing mice. The treatment process was illustrated in Fig. 7A. The ICG exposed with laser group showed unevenly tumor sizes which possibly caused by the individual differences of mice. Mice are

biologically independent samples, they have inconsistent logarithmic tumor growth cycles [55,56]. For this reason, we set 6 mice per group to avoid the possible individual differences. Tumor volume of the mice was measured every day during the treatment period. The tumor growth curves for individual mice are also shown in Fig 7B. IHNC+L (IHNC with laser irradiation) significantly inhibited the tumor growth in mice with a tumor growth inhibition rate of 79.40% on Day 16, which was approximated 2 times stronger than that of ICG (30.79%) (Fig. 7B and 7E), the tumor weight was significantly smaller than that of other groups (Fig. S20). It was excited to find that some tumors scabbed off in the IHNC+L group (Fig. 7C). Such significant tumor ablation was achieved possibly through chemotherapy in conjunction with PTT and PDT.

We further investigated the efficacy of IHNC *in vivo*. The H&E staining of major organs except the lung indicated that non-obvious pathological damage was induced in each group (Fig. S21). In lung and tumor specimens (Fig. 7D), except for the IHNC+L, compensatory expansion of the alveolar cavity caused by obvious alveolar wall thickening could be observed, indicating that combination therapy had certain anti-invasion and anti-metastasis effects. In addition, a large number of tumor cell necrosis by the treatment of IHNC+L, suggesting a typical PDT effect. TUNEL staining was used to identify apoptotic cells by detecting the breakage of nuclear DNA, the fluorescence signal (green) of apoptosis in the IHNC+L group was significantly higher (2.6 to 30.0 times) than that of other groups (Fig. 7F and 7G). In addition, there are still shortcomings in the investigation of drug efficacy. The immunogenic effect such as immunogenic cell death caused by intratumoral ROS production was rarely studied here which will be studied independently in the future.

To evaluate the primary safety of IHNC, routine blood biochemical tests were performed, and the results of tests were shown in Fig. S16C. The indicators of WBC, RBC, HGB, HCT, MCH, MCHC, MPV, and PDW were kept in the normal range and had no significant difference from the control group within 14 d The life activities of the mice in each group were normal, which further proved that the drug had no obvious biological toxicity to mice under the conditions of high-dose administration. Meantime, the hemolysis test showed no obvious hemolysis occurred with increasing drug concentration (Fig. S22A and S22B). In addition, both the IHNC and ICG groups required immobilization and laser irradiation treatment, and because of the long duration of the laser irradiation, a longer period of anesthesia was required. We used intraperitoneal injection of sodium pentobarbital (50 mg/kg) to anesthetize mice, which could have led to an impairment in eating and drinking and hence weight loss, but we were 16 d into the experiment. The average weight recovery was 95% (Fig. S23), indicating that there was no serious systemic toxicity caused by IHNC during the treatment period. We think this anesthesia do not will affect our conclusions Furthermore, we have also verified that IHNC has no significant toxic side effects through hemolysis and blood tests.

4. Conclusions

In summary, we established an amorphous nanocrystal drug complex with excellent antitumor effects and biocompatibility. Indeed, IHNC, as a highly promising tumor treatment system based on FDA-approved materials, implements the codelivery of ICG and HCPT. The ICG-based amorphous framework was designed through computer simulation. It showed the ability of loading high content of HCPT. Importantly, the prepared IHNC system was able to be *i.v.* injected and could overcome the defect of large-scale use of stabilizers. Furthermore, the nano-sized drug crystal benefited tumor accumulation and its GSH sensitivity further realized the controlled releasing behavior of HCPT in tumor cells. In the future, we are going to explore a more straightforward modification method that can achieve actively tumor targeted, and continue to conduct extensive research on the immune effects to achieve more accurate tumor treatment. In brief, the rational design of IHNC lighted a simple production manner of stabilizer-free crystalline drug injections with strong clinical application prospects.

Conflicts of Interest

We also declare that there aren't competing financial interests about the work described.

Acknowledgments

This research was financially supported by the National Key Research and Development Program of China (2021YFD1800900), National Natural Science Foundation of China (82073790), Science and Technology Research Project of Chongqing Education Commission (KJQN202100229). We are grateful to XueFeng Tang and others (Department of Pathology, Chongqing General Hospital, University of Chinese Academy of Sciences) for their help in histopathological analysis.

Supplementary materials

Supplementary material associated with this article can be found, in the online version, at doi:10.1016/j.ajps.2022.05.001.

REFERENCES

[1] Fontana F, Figueiredo P, Pei Z, Hirvonen JT, Santos HA. Production of pure drug nanocrystals and nano co-crystals by nonfinement methods. Adv Drug Deliv Rev 2018;131:3–21.
[2] Pawar VK, Singh Y, Meher JG, Gupta S, Chourasia MK. Engineered nanocrystal technology: *in-vivo* fate, targeting and applications in drug delivery. J Control Rel 2014;183:51–66.

[3] Ekladious I, Colson YL, Grinstaff MW. Polymer–drug conjugate therapeutics: advances, insights and prospects. Nat Rev Drug Discov 2019;18:273–94.
[4] Luo L, Zhang Q, Luo Y, He Z, Tian X, Battaglia G. Thermosensitive nanocomposite gel for intra-tumoral two-photon photodynamic therapy. J Control Rel 2019;298:99–109.
[5] Martin B, Seguin J, Annereau M, Fleury T, Lai-Kuen R, Neri G, et al. Preparation of parenteral nanocrystal suspensions of etoposide from the excipient free dry state of the drug to enhance *in vivo* antitumoral properties. Sci Rep 2020;10:18059.
[6] Chang TL, Zhan H, Liang D, Liang JF. Nanocrystal technology for drug formulation and delivery. Front Chem Sci Eng 2015;9:1–14.
[7] Pramanick S, Chandel V, Singodia D. Excipient selection in parenteral formulation development. Pharma Times 2013;45:65–77.
[8] Ren X, Qi J, Wu W, Yin Z, Li T, Lu Y. Development of carrier-free nanocrystals of poorly water-soluble drugs by exploring metastable zone of nucleation. Acta Pharm SinB 2019;9:118–27.
[9] Abe H, Wada H, Baghdadi M, Nakanishi S, Usui Y, Tsuchikawa T, et al. Identification of a highly immunogenic mouse breast cancer sub cell line. 4T1-S. Hum Cell 2016;29:58–66.
[10] Mahapatra LSA, Biswal B, Jena A. Formulation and evaluation of paclitaxel nanocrystals for parenteral administration by using PVP. Int J Pharma Res Health Sci 2017;5:1424–30.
[11] Schwartzberg LS, Navari RM. Safety of polysorbate 80 in the oncology setting. Adv Ther 2018;35:754–67.
[12] Blanco E, Shen H, Ferrari M. Principles of nanoparticle design for overcoming biological barriers to drug delivery. Nat Biotechnol 2015;33:941–51.
[13] Li Y, Lin J, Wang P, Luo Q, Zhu F, et al. Tumor microenvironment cascade-responsive nanodrug with self-targeting activation and ROS regeneration for synergistic oxidation-chemotherapy. Nano-micro Lett 2020;12:182.
[14] Saravanakumar G, Kim J, Kim WJ. Reactive-oxygen-species-responsive drug delivery systems: promises and challenges. Adv Sci 2017;4:1600124.
[15] Mukerabigwi JF, Yin W, Zha Z, Ke W, Wang Y, Chen W, et al. Polymersome nanoreactors with tumor pH-triggered selective membrane permeability for prodrug delivery, activation, and combined oxidation-chemotherapy. J Control Rel 2019;303:209–22.
[16] Luo L, Xu F, Peng H, Luo Y, Tian X, Battaglia G, et al. Stimuli-responsive polymeric prodrug-based nanomedicine delivering nifuroxazide and doxorubicin against primary breast cancer and pulmonary metastasis. J Control Rel 2020;318:124–35.
[17] Ling X, Tu J, Wang J, Shajii A, Kong N, Feng C, et al. Glutathione-responsive prodrug nanoparticles for effective drug delivery and cancer therapy. ACS Nano 2019;13:357–70.
[18] Yu W, Liu R, Zhou Y, Gao H. Size-tunable strategies for a tumor targeted drug delivery system. ACS Cent Sci 2020;6:100–16.
[19] Lee FY, Vessey A, Rofstad E, Siemann DW, Sutherland RM. Heterogeneity of glutathione content in human ovarian cancer. Cancer Res 1989;49:5244–8.
[20] Liu JJ, Wu M, Pan YT, Duan YK, Dong ZL, Chao Y, et al. Biodegradable nanoscale coordination polymers for targeted tumor combination therapy with oxidative stress amplification. Adv Funct Mater 2020;30:1908865.
[21] Junyaprasert VB, Morakul B. Nanocrystals for enhancement of oral bioavailability of poorly water-soluble drugs. Asian J Pharm Sci 2015;10:13–23.
[22] Liu Y, Lv S, Liu D, Song F. Recent development of amorphous metal coordination polymers for cancer therapy. Acta Biomater 2020;116:16–31.
[23] Rezaei M, Abbasi A, Dinarvand R, Jeddi-Tehrani M, Janczak J. Design and synthesis of a biocompatible 1D coordination polymer as anti-breast cancer drug carrier, 5-Fu: *in vitro* and *in vivo* studies. ACS Appl Mater 2018;10:17594–604.
[24] Yu Y, Liu J, Chao L, Feng L, Zhuang L. Nanoscale metal-organic particles with rapid clearance for MR imaging guided photothermal therapy. ACS Nano 2016;10:2774–81.
[25] Horcajada P, Gref R, Baati T, Allan PK, Maurin G, Couvreur P, et al. Metal organic frameworks in biomedicine. Chem Rev 2012;112:1232.
[26] Fan Z, Liu H, Xue Y, Lin J, Fu Y, Xia Z, et al. Reversing cold tumors to hot: an immunoadjuvant-functionalized metal-organic framework for multimodal imaging-guided synergistic photo-immunotherapy. Bioact Mater 2021;6:312–25.
[27] Ma R, Alifu N, Du Z, Chen S, Heng Y, Wang J, et al. Indocyanine green-based theranostic nanoplatform for NIR fluorescence image-guided chemo/photothermal therapy of cervical cancer. Int J Nanomed 2021;16:4847–61.
[28] Fan H, Chen S, Du Z, Yan T, Alimu G, Zhu L, et al. New indocyanine green therapeutic fluorescence nanoprobes assisted high-efficient photothermal therapy for cervical cancer. Dyes Pigm 2022;200:110174.
[29] Yang Y, Chao Y, Liu J. Core-shell and co-doped nanoscale metal-organic particles (NMOPs) obtained via post-synthesis cation exchange for multimodal imaging and synergistic thermo-radiotherapy. NPG Asia Mater 2017;9:e344.
[30] Lin H, Li S, Wang J, Chu C, Zhang Y, Pang X, et al. A single-step multi-level supramolecular system for cancer sonotheranostics. Nanosc Horiz 2019;4:190–5.
[31] Guo J, Tardy BL, Christofferson AJ, Dai Y, Richardson JJ, Zhu W, et al. Modular assembly of superstructures from polyphenol-functionalized building blocks. Nat Nanotechnol 2016;11:1105–11.
[32] Duren T, Millange F, Ferey G, Walton KS, Snurr RQ. Calculating geometric surface areas as a characterization tool for metalorganic frameworks. J Phys Chem C 2016;111:15350–6.
[33] Zhang L, Zhang F, Yang X, Long G, Wu Y, Zhang T, et al. Porous 3D graphene-based bulk materials with exceptional high surface area and excellent conductivity for supercapacitors. Sci Rep 2013;3:1408.
[34] Collins JT, Kuppe C, Hooper DC, Sibilia C, Centini M, Valev VK. Chirality and chiroptical effects in metal vanostructures: fundamentals and current trends. Adv Opt Mater 2017;5:1700182.
[35] Long G, Sabatini R, Saidaminov MI, Lakhwani G, Rasmita A, Liu X, et al. Chiral-perovskite optoelectronics. Nat Rev Mater 2020;5:423–39.
[36] Fontana F, Figueiredo P, Pei Z, Hirvonen JT, Santos HA. Production of pure drug nanocrystals and nano co-crystals by confinement methods. Adv Drug Deliv Rev 2018;131:3–21.
[37] Thakral S, Terban MW, Thakral NK, Suryanarayanan R. Recent advances in the characterization of amorphous pharmaceuticals by X-ray diffractometry. Adv Drug Deliv Rev 2016;100:183–93.
[38] Auerbach M, Deloughery T. Single-dose intravenous iron for iron deficiency: a new paradigm. Hematol Am Soc Hematol Educ Program 2016;2016:57–66.
[39] Tefferi A. How we diagnose and treat iron deficiency anemia. Am J Hematol 2016;91:31–8.
[40] Rampton D, Folkersen J, Fishbane S, Hedenus M, Weiss G. Hypersensitivity reactions to intravenous iron: guidance for risk minimization and management. Haematologica 2014;99:1671–6.

[41] Mahbubul IM. Stability and dispersion characterization of nanoflui. Preparation, characterization, properties and application of nanofluid. William Andrew Publishing; 2019. p. 47–112.
[42] Ianevski A, He L, Aittokallio T, Tang J. SynergyFinder: a web application for analyzing drug combination dose-response matrix data. Bioinformatics 2017;33:2413–15.
[43] Güvenç Paltun B, Kaski S, Mamitsuka H. Machine learning approaches for drug combination therapies. Brief Bioinform 2021;293:1477–4054.
[44] Chou TC. Theoretical basis, experimental design, and cmputerized simulation of synergism and antagonism in drug combination studies. Pharmacol Rev 2006;58:621–81.
[45] Golombek SK, May JN, Theek B, Appold L, Drude N, Kiessling F, et al. Tumor targeting via EPR: strategies to enhance patient responses. Adv Drug Deliv Rev 2018;130:17–38.
[46] Shen G, Xing R, Zhang N, Chen C, Ma G, Yan X. Interfacial cohesion and assembly of bBioadhesive molecules for design of long-term stable hydrophobic nanodrugs toward effective anticancer therapy. ACS Nano 2016;10:5720–9.
[47] Liu J, Yuan X, Deng L, Yin Z, Tian X, Bhattacharyya S, et al. Graphene oxide activated by 980nm laser for cascading two-photon photodynamic therapy and photothermal therapy against breast cancer. Appl Mater Today 2020;20:100665.
[48] Li Y, Zhao P, Gong T, Wang H, Bu W. Redox dyshomeostasis strategy for hypoxic tumor therapy based on DNAzyme-loaded electrophilic ZIFs. Angew Chem 2020;59:22537–43.
[49] Adler J, Parmryd I. Colocalization analysis in fluorescence microscopy. Methods Mol Biol 2013;931:97–109.
[50] Sheng Z, Hu D, Zheng M, Zhao P, Liu H, Gao D, et al. Smart human serum albumin-indocyanine green nanoparticles generated by programmed assembly for dual-modal imaging-guided cancer synergistic phototherapy. ACS Nano 2014;8:12310–22.
[51] Zheng M, Yue C, Ma Y, Gong P, Zhao P, Zheng C, et al. Single-step assembly of DOX/ICG loaded lipid–polymer nanoparticles for highly effective chemo-photothermal combination therapy. ACS Nano 2013;7:2056–67.
[52] Fu W, Zhang X, Mei L, Zhou R, Yin W, Wang Q, et al. Stimuli-responsive small-on-large nanoradiosensitizer for enhanced tumor penetration and radiotherapy sensitization. ACS Nano 2020;14:10001–17.
[53] Shao J, Xie H, Huang H, Li Z, Sun Z, Xu Y, et al. Biodegradable black phosphorus-based nanospheres for *in vivo* photothermal cancer therapy. Nat Commun 2016;7:12967.
[54] Li Z, Huang H, Tang S, Li Y, Yu XF, Wang H, et al. Small gold nanorods laden macrophages for enhanced tumor coverage in photothermal therapy. Biomaterials 2016;74:144–54.
[55] Fujiwara Y, Torphy RJ, Sun Y, Miller EN, Ho F, Borcherding N, et al. The GPR171 pathway suppresses T cell activation and limits antitumor immunity. Nat Commun 2021;12:5857.
[56] Kim J, Francis DM, Sestito LF, Archer PA, Manspeaker MP, O'Melia MJ, et al. Thermosensitive hydrogel releasing nitric oxide donor and anti-CTLA-4 micelles for anti-tumor immunotherapy. Nat Commun 2022;13:1479.